

Chapter 2 Flows of the Near-Surface Boundary Layer

Wind shear near the surface is responsible for the entrainment of sand particles, the formation and evolution of aeolian landforms, and the disasters induced by wind-blown sand movement. Therefore, many studies of the wind-blown sand movement are focused on understanding, representing and depicting the characteristics of air flows in the near-surface boundary layer where the wind-blown sand movement mainly takes place. The content of this chapter is arranged as follows. In Sects. 2.1 and 2.2, some basic definitions and equations, including the turbulent model, relevant to the wind-blown sand movement, are introduced in the light of fluid dynamics; Sects. 2.3 and 2.4 provide a brief summary of the characteristics and major observation methods of the atmospheric boundary layer, especially the near-surface boundary layer; Sect. 2.5 gives the basic equations governing air flow and their simplified forms for the near-surface layer and the wind-blown sand movement; Based on field observational results on the surface wind gusts, Sect. 2.6 devotes to the analysis on the statistical characteristics of fluctuating wind fields and resultant saltation activity near the surface, and then to establish two wind velocity prediction models to describe variations of fluctuating wind velocity at different heights and times.

2.1 An Introduction to Fluid Mechanics

As a rigorous discipline, fluid mechanics, especially fluid dynamics, came into being based on basic concepts and equations of velocity, acceleration, force, fluid field etc. and the fundamental laws which relate to the conservations of mass, momentum and energy. A fluid is usually assumed to be composed of (fluid) volume elements, which are assumed to be infinitely small from a macroscopic view and enormous from a microscopic view and among which no static friction exists. In this manner, the influence of molecular motions could be ignored and the property of a fluid could be regarded as continuous and isotropic. There are two ways to describe the fluid motion: the Euler and the Lagrange method. The former describes the

fluid motion within a given space or at a fixed point, while the latter traces the motion of specific particles of fluid. In the following part, without further specification, the Euler description of fluid motion is employed.

2.1.1 Viscosity of a Fluid

The viscosity of a fluid behaves like a drag effect caused by internal friction between two adjacent fluid layers where relative motion happens. It is a property that connects the shear stress and the velocity gradient of a fluid, and is one of the reasons for energy dissipation in a moving fluid. Viscosity can be denoted by the viscosity coefficient μ (measured in Pa·s). For gas, it is usually taken as 1.81×10^{-5} Pa·s, which increases with temperature increases but is almost unaffected by air pressure. Another important indicator for the effect of fluid viscosity is the Reynolds Number which is defined as the ratio of inertial force to viscous force: $Re = \rho UL / \mu$, where ρ , U and L are fluid density, characteristic velocity and characteristic length respectively. The smaller the Reynolds number is, the greater the viscous force's influence will be.

According to the magnitude and importance of viscosity in the problem under discussion, a fluid can be considered as an ideal fluid or a viscous fluid. A fluid is said to be ideal in the case that viscosity or relative velocity of the fluid motion is comparatively small, so its viscous stress could be ignored in comparison with other forces. It is notable that the ideal fluid is merely an approximation model of the real fluid under these conditions. In contrast, if its viscous stress cannot be ignored, it is a viscous fluid.

Viscous fluids can be further classified into Newtonian fluids and non-Newtonian fluids. A fluid is called Newtonian when it meets Newton's law of viscosity, that is, the internal friction shear stress between two fluid layers is in proportion to the relative velocity of the two layers where the ratio μ is a constant. Otherwise, it is a non-Newtonian fluid. In general, air and water are both considered as Newtonian fluids; while fluid, suspensions, liquid, polymer solution, blood and mud-rock flow in nature should be considered as non-Newtonian fluids. Air flow in the wind-blown sand flow can be regarded as Newtonian fluid.

2.1.2 Properties of Flow

Fluid mechanics deals with both incompressible and compressible fluids, that is, with fluids of either constant or variable density. Although there is no such thing in reality as an incompressible fluid, this term is applied

where the change in density with pressure is so small as to be negligible. This is usually the case with liquids. Gases, too, could be considered incompressible when the pressure variation is small in comparison with the absolute pressure. So air flow in the wind-blown sand flow can also be regarded as incompressible flow.

Fluid flow can also be divided into steady and unsteady. A steady flow is the one in which physical quantities, such as velocity, pressure, temperature and density could vary from point to point but do not change with time. At a given point, if conditions do change with time, the flow is described as unsteady. In practice, there will always be slight local variations of velocity and pressure, but if the average of these quantities is constant, the flow is considered to be steady, such as flow in the pipe or the boundary layer.

According to the state of fluctuation of physical quantities during the fluid's motion, the flow could be divided into turbulent and laminar flow. The fundamental characteristic of turbulence is the randomness of the motion of fluid volume elements. For turbulence, the instantaneous value of every local quantity, such as velocity u , pressure P , temperature T , concentration c and so on, can be expressed as the sum of a mean component and a fluctuating component due to turbulence while the mean of fluctuating component is zero. The flow is laminar flow if the viscous fluid travels smoothly or in regular paths. Laminar flow occurs only when the Reynolds number is small. When the Reynolds number exceeds a certain critical value (the turning point), laminar flow begins to transit into turbulence. In general, the analysis of laminar flow is far easier than turbulent since the equations of laminar flow have exact or approximate solutions.

Turbulence predominates in most flows in nature and engineering applications, whose major effects are an intensive transportation of momentum, heat and mass caused by random fluctuations. Turbulence contains eddies of diversified scales. The unstable large eddies give birth to smaller ones and the process repeats itself. This is called 'cascade' process. Since there are large eddy structures within it, turbulence is often regarded as irregular fluid motions with structures of diversified sizes. Though the turbulent value is spatially and temporally random, turbulent quantities still behaves as a physical continuum and is governed by the basic equations of fluid motion.

The turbulence is characterized by diffusion, dissipation, correlation, self-similarity and intermittency. Here, correlation indicates the interdependence between turbulent motions at different point of time or space. This degree of interdependence is inclined to decrease to zero as the temporal or spatial distance increases. Turbulent self-similarity indicates the self-similarity between eddies of different scales. These self-similar struc-

tures obey a scaling law; that is, in some certain areas of wave number space or on some physical scales, some quantities, such as the velocity structure function, are in direct proportion to fixed powers of other physical quantities. It is notable that the Navier-Stokes equations also meet scale invariance law. Turbulent intermittency makes the geometrical image of the turbulent movement fragile, for example, when the turbulent flow is confined, the boundary between the turbulent area and the non-turbulent area is irregular and is susceptible to fractals at any time. Moreover, the turbulence is a ‘burst’ process and has a large-scale eddy structure. The ‘burst’ process usually occurs in the viscous layer and buffer layer. Kline et al. (1967) found that, in the direction of flow, there naturally exist alternatively distributed low and high velocity stripes in the near wall area. The low velocity stripes gradually move downstream, moving further away from the wall and upward. Having reached the buffer layer, the stripes vibrate violently and eventually break into small-scale structures. This process is the so called ‘burst’ process. After the upcast of the low velocity stripes, the upper high velocity fluid volume elements subside rapidly. Large eddies in the boundary layer causes this burst to subsidence process, which is named by Kline et al. (1967) as coherent structure exhibit this process.

For atmospheric boundary layer flows, $Re \approx 10^8$ (Wyngaard 1992). Hence the atmospheric boundary layer flows are almost always turbulent. When the wind velocity in the open air exceeds $1 \text{ m}\cdot\text{s}^{-1}$, the air movement must be turbulent, no matter how smoothly the wind seems to pass by (Bagnold 1941). Therefore, the air flows which cause moving sand in the near surface layer are nearly all turbulent (Pettijohn et al. 1972) and exert a great influence on the material transportation and deposit. A detailed and comprehensive description of the irregularity and complexity of the turbulent movement is always the object scientists strive for. Any interested reader may be better informed by Frisch (1995).

2.2 Basic Equations of Fluid Mechanics

In this section, the three basic conservation laws of mass, momentum and energy are given first. Then, due to the importance of turbulence in the studies of wind-blown sand movement, basic governing equations, major patterns and several numerical simulation approaches to turbulence are briefly introduced. Due to the complexity of fluid motion and the limited space of this book, the theories of fluid mechanics could only be sketched; interested readers may refer to Landau and Lifshitz (1987).

2.2.1 Conservation of Mass (Continuity Equation)

Any closed flow system must satisfy the conservation of mass, that is, the rate of change of the mass of the fluid (with density ρ and volume V) with time t is equal to the total mass of the fluid passing through the boundary S , i.e.,

$$\frac{\partial}{\partial t} \int_V \rho dV = - \oint_S \rho \mathbf{u} \cdot d\mathbf{S} \quad \text{or} \quad \frac{\partial \rho}{\partial t} = -\nabla \cdot (\rho \mathbf{u}). \quad (2.1)$$

For steady flow, the density ρ is unaffected by time, namely,

$$\nabla \cdot (\rho \mathbf{u}) = 0. \quad (2.2)$$

For incompressible flow, the density ρ is a constant, and then the above equation takes the following form,

$$\nabla \cdot \mathbf{u} = 0 \quad \text{or} \quad \frac{\partial u_i}{\partial x_i} = 0, \quad (2.3)$$

where, $\nabla = (\partial/\partial x_i) \mathbf{e}_i$ is the divergence operator; $\mathbf{u} = u_i \mathbf{e}_i$ is the velocity vector of fluid material elements; \mathbf{e}_i is the unit vector of the coordinates $Ox_1x_2x_3$ and u_i is the component of the velocity vector in direction \mathbf{e}_i . According to Einstein's summation convention, when a subscript occurs more than once in the same expression, the expression is implicitly summed over all possible values for that index, so $i = 1, 2, 3$ or $x_i = x_1, x_2, x_3$.

2.2.2 Conservation of Momentum

Any closed flow system must also conserve momentum, that is, the rate of change of the momentum of the fluid (with density ρ and volume V) with time is equal to the sum of momentum of fluid passing through boundary S , the total power of the body force \mathbf{f} acting on unit mass and the surface force \mathbf{T}_n acting on S , that is,

$$\frac{\partial}{\partial t} \int_V (\rho \mathbf{u}) dV = - \oint_S \rho \mathbf{u} (\mathbf{u} \cdot \mathbf{n}) dS + \int_V \rho \mathbf{f} dV + \oint_S \mathbf{T}_n dS. \quad (2.4)$$

The corresponding differential equation is

$$\frac{d\rho \mathbf{u}}{dt} = \frac{\partial \rho \mathbf{u}}{\partial t} + \nabla \cdot (\rho \mathbf{u}) = \rho \mathbf{f} + \nabla \cdot (T_{ij} \mathbf{e}_i \mathbf{e}_j), \quad (2.5)$$

where \mathbf{n} is the unit vector in the normal direction of the boundary S , and $T_{ij} = (-P + \mu' S_{kk})\delta_{ij} + \tau_{ij}$ is the surface stress tensor acting on the fluid volume element. Here P is the pressure on the fluid volume element, δ_{ij} is the unit tensor, $\mu' S_{kk}\delta_{ij}$ is the stress tensor caused by volume change; viscous stress tensor $\tau_{ij} = \mu S_{ij}$, $S_{ij} = \partial u_i / \partial x_j + \partial u_j / \partial x_i$ is the deformation rate caused by the fluid motion, μ' is the second viscosity coefficient, generally taken as $\mu' = -2\mu/3$. Substituting the expression T_{ij} (the constitutive relation of Newton's fluid) into the differential equation of the momentum conservation (i.e., Eq. 2.5), the N-S equation can be written as

$$\rho \left(\frac{\partial u_i}{\partial t} + u_j \frac{\partial u_i}{\partial x_j} \right) = -\frac{\partial P}{\partial x_i} + \mu \frac{\partial}{\partial x_k} \left(\frac{\partial u_i}{\partial x_j} + \frac{\partial u_j}{\partial x_i} \right) - \frac{2}{3} \mu \frac{\partial^2 u_k}{\partial x_i \partial x_k} + \rho f_i. \quad (2.6)$$

For incompressible flow, it reduces to the following form

$$\rho \left(\frac{\partial u_i}{\partial t} + u_j \frac{\partial u_i}{\partial x_j} \right) = -\frac{\partial P}{\partial x_i} + \mu \nabla^2 u_i + \rho f_i. \quad (2.7)$$

2.2.3 Conservation of Energy

The conservation of energy is also a basic law that a flow system of heat exchange must satisfy. It is actually the first law of thermodynamics which can be expressed as: the increase rate of the volume element's energy is equal to the sum of the net heat flux entering the element, or q_T , and the power of the body force and surface force acting on the volume element, namely,

$$\rho \frac{\partial}{\partial t} \left(e + \frac{u^2}{2} \right) + \rho u_j \frac{\partial}{\partial x_j} \left(e + \frac{u^2}{2} \right) = \rho f_i u_i + \frac{\partial}{\partial x_i} (T_{ij} u_j) + \rho \dot{q}_T + \lambda_T \nabla^2 T, \quad (2.8)$$

where, e is the internal energy of unit mass, the first two terms in the right part are power made by body force and surface force respectively, \dot{q}_T is the heat source term, $\lambda_T \nabla^2 T$ is the heat conduction term, in which T is Kelvin temperature and λ_T is the thermal conductivity. Since the internal energy is related to temperature, $e = c_p T$, where c_p is the heat capacity at constant pressure, for incompressible flow, the energy conservation equation with respect to T is expressed in the following form

$$\rho \left(\frac{\partial T}{\partial t} + u_j \frac{\partial T}{\partial x_j} \right) = \frac{\lambda_T}{c_p} \nabla^2 T + S_T, \quad (2.9)$$

where S_T is the viscous dissipation term which includes the inner thermal source and the thermal energy, into which the mechanical energy turns due to the viscous effect. To make the equations closed, a state equation connecting pressure P and density ρ , $P=P(\rho, T)$, is required. For an ideal gas, $P=\rho RT$, where R is the Molar gas constant.

2.2.4 Basic Equations of Turbulence

It is generally assumed that no matter how complicated turbulence is, its instantaneous motion is still subject to unsteady conservation of mass equation (i.e., Eq. 2.1) and the N-S equation (i.e., Eq. 2.5). The popular approach to studying turbulent motion is the time-averaged method, that is, the turbulence is considered as a combination of two flow movements, the time-averaged flow and instantaneous turbulent flow. The most widely used time-averaged method is the Reynolds-averaged method. Here, the superscript ‘ $-$ ’ stands for the mean of a physical quantity within a time period Δt ; ‘ $'$ ’ stands for a physical quantity’s fluctuation. Ignoring the density fluctuation but taking into consideration the change of the mean density, the averaged control equations for turbulence could be obtained from Eqs. 2.1 and 2.5. These are respectively the time-averaged continuity equation and the N-S equation for compressible flow, namely,

$$\frac{\partial \rho}{\partial t} + \frac{\partial(\rho \bar{u}_j)}{\partial x_j} = 0, \quad (2.10)$$

$$\rho \left(\frac{\partial \bar{u}_i}{\partial t} + \bar{u}_j \frac{\partial \bar{u}_i}{\partial x_j} \right) = -\frac{\partial \bar{P}}{\partial x_i} + \mu \frac{\partial^2 \bar{u}_i}{\partial x_j^2} - \rho \frac{\partial \overline{u'_i u'_j}}{\partial x_j} + \rho \bar{f}_i. \quad (2.11)$$

As the Reynolds averaged method is employed, Eq. 2.11 is also called the Reynolds time-averaged Navier-Stokes equation. In which $-\rho \overline{u'_i u'_j}$ is called the Reynolds stress, a new quantity relevant to turbulent fluctuation which changes the original closed equation into a non-closed one. Therefore, it is necessary to make some assumptions for the Reynolds stress, i.e., constructing an expression for the stress or introducing a new turbulent model equation, so as to connect the turbulent fluctuation value with its time-averaged value and hence close the equations.

2.2.5 Models of Turbulence

According to the assumptions made for the Reynolds stress, the turbulent model can be divided into the Reynolds stress model and the eddy viscos-

ity model. In the former case, the function indicating the Reynolds stress is directly constructed and then solved together with the averaged control equations for turbulence (i.e., Eqs. 2.10 and 2.11). In the latter case, a quantity of turbulent viscosity or eddy viscosity coefficient μ_t is introduced as a spatial coordinate function related to flow state rather than as a physical parameter, and is connected with the time-averaged turbulence parameters. This relationship is called the eddy viscosity model. According to Boussinesq's eddy viscosity model, the relationship between the Reynolds stress and the mean velocity gradient is written as

$$-\rho \overline{u'_i u'_j} = \mu_t \left(\frac{\partial \overline{u}_i}{\partial x_j} + \frac{\partial \overline{u}_j}{\partial x_i} \right) - \frac{2}{3} \left(\rho K + \mu_t \frac{\partial \overline{u}_k}{\partial x_k} \right) \delta_{ij}, \quad (2.12)$$

with $K = \overline{u'_i u'_i} / 2$. The key point of calculating a turbulent flow is to determine the turbulent kinetic viscosity μ_t . Several modes have been proposed and according to the number of differential equations required to determine μ_t , the eddy viscosity models were divided into the zero-equation model, the one-equation model and the two-equation model.

The zero-equation model employs algebraic relations, rather than differential equations to connect the turbulent kinetic viscosity and the time-averaged turbulent parameters. The most well-known zero-equation model is Prandtl's mixing length theory, from which calculated results agree well with experiments for simple flow cases, but seemingly not so well for complex flow. To compensate for the limitations of the zero-equation model, the one-equation model is proposed. It works like this: on the basis of the averaged control equation for turbulence equation (see Eq. 2.11), a turbulent kinetic energy transport equation is constructed to represent μ_t as a function of the turbulent kinetic energy K , $\mu_t = \rho C_\mu \sqrt{K} l$, where C_μ is a empirical constant and l is the proportional length of the turbulent fluctuation. In this manner, the equations are closed. The turbulent kinetic energy transport equation can be expressed as

$$\frac{\partial K}{\partial t} + \overline{u}_j \frac{\partial K}{\partial x_j} = \frac{1}{\rho} \frac{\partial}{\partial x_j} \left[\left(\mu + \frac{\mu_t}{\sigma_k} \right) \frac{\partial K}{\partial x_j} \right] + \frac{\mu_t}{\rho} \frac{\partial \overline{u}_i}{\partial x_j} \left(\frac{\partial \overline{u}_i}{\partial x_j} + \frac{\partial \overline{u}_j}{\partial x_i} \right) - \frac{\rho}{l} C_d K^{\frac{3}{2}}, \quad (2.13)$$

where σ_k is the Prandtl number of the fluctuation momentum; the values of σ_k and C_μ will be given in the following part. As to the value of C_d , one can refer to Launder and Spalding (1972).

To solve Eq. 2.13, l should be determined in advance, but this is not an easy task. Therefore, the one-equation model is not widely used in practice. To solve this problem, the K - ε model is put forward. Based on the one-equation model, a new equation with the turbulent dissipation rate

$\varepsilon = \nu(\overline{\partial u'_i / \partial x_j})^2$ is introduced where $\nu = \mu / \rho$ as the kinetic viscous coefficient. In this way, the turbulent kinetic viscosity μ_t can be expressed as a function of the turbulent kinetic energy K and the turbulent dissipation rate ε : $\mu_t = \rho C_\mu K^2 / \varepsilon$. Therefore, the transport equations relative to K and ε can be expressed as

$$\frac{\partial K}{\partial t} + \bar{u}_j \frac{\partial K}{\partial x_j} = \frac{1}{\rho} \frac{\partial}{\partial x_j} \left[\left(\mu + \frac{\mu_t}{\sigma_k} \right) \frac{\partial K}{\partial x_j} \right] + \frac{1}{\rho} \mu_t \frac{\partial \bar{u}_i}{\partial x_j} \left(\frac{\partial \bar{u}_i}{\partial x_j} + \frac{\partial \bar{u}_j}{\partial x_i} \right) - \varepsilon, \quad (2.14)$$

$$\frac{\partial \varepsilon}{\partial t} + \bar{u}_j \frac{\partial \varepsilon}{\partial x_j} = \frac{1}{\rho} \frac{\partial}{\partial x_j} \left[\left(\mu + \frac{\mu_t}{\sigma_\varepsilon} \right) \frac{\partial \varepsilon}{\partial x_j} \right] + \frac{\mu_t C_{1\varepsilon} \varepsilon}{\rho K} \frac{\partial \bar{u}_i}{\partial x_j} \left(\frac{\partial \bar{u}_i}{\partial x_j} + \frac{\partial \bar{u}_j}{\partial x_i} \right) - \frac{C_{2\varepsilon} \rho \varepsilon^2}{K}, \quad (2.15)$$

where $C_{1\varepsilon} = 1.44$, $C_{2\varepsilon} = 1.92$, $C_\mu = 0.09$, $\sigma_k = 1.0$, $\sigma_\varepsilon = 1.3$ recommended by Launder and Spalding (1972) and proved by later experiments. Eqs. 2.14 and 2.15 are called the standard K - ε model. This is currently the most widely used turbulent model.

The standard K - ε model is much more advanced than the zero- and one-equation models and it is widely and successfully used in scientific studies and engineering applications. However, it suffers distortions to some extent when treating flows with strong swirling, the flows near curved wall or flows with curved streamlines. Therefore, some improved versions of the K - ε model, such as the renormalization group (RNG) K - ε model, and the Realizable K - ε model have been derived. Generally speaking, either the mixing length or one-equation model is advisable for simple flow cases, such as flow in the boundary layer, jet flow, pipe flow or flow in a channel without rotation, recirculation or buoyancy; while the K - ε model or the other two-equation models may be more suitable to non-buoyancy recirculating, irrotational or weakly rotational flow. A more sophisticated model (see Yakhot and Orzag 1986; Moin 1997) is needed to tackle flows with strong swirling and buoyancy or compressible flows. In short, the selection of model depends on the characteristics of the specific problem under discussion.

2.2.6 Approaches of Turbulent Numerical Simulation

Though basic equations describing the turbulent motion have been established, it's not an easy task to solve them analytically. Therefore, at present numerical approaches are generally employed. Some sophisticated numerical models have been proposed to understand the physical properties of turbulence. Among which, the Direct Numerical Simulation (DNS)

model is of the most accuracy. It solves the instantaneous turbulent control equations (i.e., Eqs. 2.1 and 2.6) directly. When only the statistical quantities of turbulence are concerned, the numerical calculation can be accomplished by introducing the corresponding closed form model into the turbulent averaged control equation (i.e., Eq. 2.11), to form the so-called Reynolds-Averaged Navier-Stokes (RANS) model. Though practical, the closed RANS model is not universal since Reynolds stress mainly originates from the large-scale fluctuation and its properties are closely related to the boundary condition of the flow. In other words, there does not exist a uniform model which can be applied to all complex flows. As far as computational complexity is concerned, the Large Eddy Simulation (LES) model lies between the DNS and the RANS model. It works like this: the large-scale fluctuation or turbulent eddies are calculated through numerical simulation and the impact of the small-scale eddies on the large-scale ones is modeled on the basis of some conceptual, for example, the sub-grid scale (SGS) model. The Large Eddy Simulation model was first put forward by Smagorinsky (1963) and was then developed by other researchers into more sophisticated versions, such as the Lagrange dynamical model proposed by Meneveau et al. (1996) for non-isotropic turbulence. The main motivation behind the LES model stems from local balance of small scale fluctuation which may be subjected to some kind of locally applicable laws, such as local isotropy or local similarity.

The three numerical models mentioned above require substantially different resolutions of the flow field. The DNS model calculates turbulent fluctuations of all scales and the minimum resolution in algorithm must be smaller than the dissipation scale. The RANS gives an average of the Reynolds stresses generated by fluctuation of all scales, and the grid scale must be larger than the fluctuation integral scale or the length scale of energy containing eddies, and its minimum grid scale is also determined by the properties of mean flow. The resolution of LES lies between those of DNS and RANS. Its grid scale should be of the same order of magnitude of the scale of the inertial sub-region, since only the fluctuations smaller than the scale of the inertial sub-region may possibly be subjected to a locally applicable law.

2.3 Basic Characteristics of the Atmospheric Boundary Layer

The atmosphere is a layer of gases covering the Earth's surface, which is composed of nitrogen, oxygen and suspension particles (aerosol). It re-

volves together with the Earth and its density decreases with height. Energy needed for atmospheric motion mainly comes from solar radiation. The latitudinal heat imbalance drives global large-scale atmospheric motion – the global atmospheric circulation; meanwhile, in a localized area the heat imbalance causes regional atmospheric convection and turbulence. The latter is characterized by a high Reynolds Number, which can be decomposed into multi-scale fluctuations or eddies of various scales down to the viscous dissipation scale. Consequently, atmospheric motion is characterized by temporal and spatial multi-scale and dissipation, and thus, generally speaking, the atmospheric system is a system of dissipative structure.

According to the characteristics of temperature distribution with height, the atmosphere can be divided into four layers: the troposphere, the stratosphere, the mesosphere and the thermosphere (see Fig. 2.1). Generally speaking, the troposphere layer over equatorial and tropical areas is of 15–20 km in depth, while that over polar and middle latitudes is of 8–14 km in depth. Compared with the whole atmosphere, the troposphere is very thin but contains 75% of the atmospheric mass and nearly all moisture, cloud and precipitation. Most synoptic events, such as cold waves, typhoon,

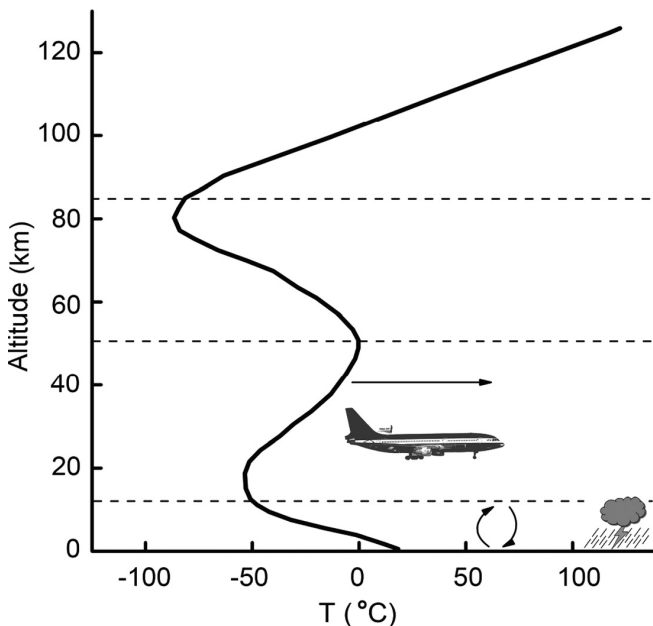


Fig. 2.1. Stratification of the atmosphere, the layers are respectively called troposphere, stratosphere, mesosphere and thermosphere with increasing altitude

thunder storms and lightning take place in the troposphere layer. It has the following features:

- (1) Decrease of temperature with height at a mean rate of about $6.5 \text{ K}\cdot\text{km}^{-1}$. The atmosphere absorbs heat through long-wave radiation, convection and turbulence from the ground and so the closer it is to the ground, the more heat it absorbs. This property gives birth to intensive convective motions within the troposphere and will facilitate the vertical transport of atmospheric components, such as vapor and aerosol.
- (2) Strong vertical mixing. Because of the influence of heating at the Earth surface, the warmer air at low altitudes rises while the colder air at high altitude sinks. This produces strong vertical mixing in the troposphere layer, and the maximum upward-velocity can reach up to $20\text{--}30 \text{ m}\cdot\text{s}^{-1}$. This is always associated with severe convection weathers, such as thunder storm, tornados, hail or squall lines.
- (3) Unbalanced horizontal distribution of meteorological elements. Due to the diversity in latitude and characteristic of the land surface, air over the ground is of different physical properties. The horizontal imbalance of pressure, temperature, humidity etc., in turn, produces various synoptic events.

The bottom of the troposphere ranging from the ground surface to an altitude of 1000 m has a sustained wind and temperature vertical gradient in response to the Earth's surface friction and surface heating. This is the so-called atmospheric boundary layer (ABL). Above it, the effect of earth's surface friction on air motion is negligible and that is where the free atmosphere performs. In the free atmosphere, the pressure gradient and the Coriolis forces dominate the behaviour of the flow field and induce the geostrophic wind, which is at an angle ($<30^\circ$) to the wind in the ABL. It should be pointed out that the atmospheric boundary layer is different from the boundary layer fluid mechanics. The concept of 'boundary layer' was first introduced by Prandtl to study the fluid motion with a large Reynolds number. He believed that in a thin layer near the wall the fluid's viscous force is of a large gradient in the direction perpendicular to the wall, and its effects cannot be ignored in comparison with the inertial force. Since the velocity of flow gradually changes from the boundary layer to the external layer, the thickness of the boundary layer is defined as the vertical distance from the wall to the place where the fluid velocity can reach 99% of the free velocity. Additionally, since there is exchange of momentum and mass between the atmospheric boundary layer flow field and the external non-viscous flow field, the flow velocity in the atmospheric boundary layer is related to both the horizontal coordinate x and the vertical z .

For different underlying surfaces, like desert, soil, vegetation, cities, water, etc. It has different physical properties, such as different radiation properties, thermal capacities, moisture content and roughness, all of which will exert different influences on the atmospheric motion and cause different stratifications and atmospheric boundary layer conditions.

The atmospheric boundary layer can be divided into the viscous subsidiary layer, the surface layer and the upper friction layer (or Ekman layer). The viscous subsidiary layer is a thin layer close to the surface, where the molecular viscosity is much larger than the turbulent shear stress. The viscous subsidiary layer includes the laminar flow region and transitional region. As it approaches to the wall, the viscous stress gradually dominates the flow. However, in practice its typical thickness is less than 1 cm and can be ignored. The space from the viscous subsidiary layer to 50–100 m height above the Earth's surface is the surface layer, where the atmospheric motion is typically turbulent and the turbulent momentum flux is approximately constant. So the layer is also called the constant flux layer. In the surface layer, the wind direction is unchangeable with height, while above it wind velocity increases with height and wind direction deflects constantly because of the weakening of the surface friction effect, until the flow field is completely dominated by the pressure gradient and the Coriolis force, and the combined actions of which result in the wind direction tending towards the direction of the geostrophic wind, and thus forming the famous 'Ekman spiral'. Wind direction changes continually to the top of the Ekman layer. Moreover, the atmospheric layer below 2 m is the near-surface layer. It is characterized by a large velocity gradient and a logarithmic wind profile, for the flow field is greatly influenced by the wall surface and the influence of thermal factors is negligible compared with dynamic factors. As far as the wind-blown sand movement is concerned, the motion of saltating sand takes place within 10 cm above the surface, therefore, the wind field in the near-surface layer plays a crucial role in sand particles' movement.

The air motion in the ABL is almost always turbulent (above 5–10 cm). The turbulence intensity could reach up to 20%. Due to surface radiation, air stratification alternates between stable and instable states, causing the diversified mean wind velocity profiles and turbulent characteristics to vary. Moreover, the non-uniform topography and covering condition also complicate the air flow in the boundary layer, especially the surface layer. Under the influence of the temporal and spatial changes of wind field and its strong turbulent characteristics, the state of erosion and deposit of the surface material vary with wind field and topography accordingly. Therefore, the quantities indicating material transportation in different experi-

ments differ greatly, which poses tremendous obstacles to the wind-blown and movement studies.

2.4 Observations of the Atmosphere Boundary Layer

The knowledge of atmospheric boundary layer is mainly obtained from experimental observation, which includes filed measurement and laboratory simulation. The former can be performed with the help of ground measurement, tower (Fig. 2.2a), released or tethered balloon (Fig. 2.3), aerial photography and remote sensing technology, while the latter mostly use wind tunnels. In recent years, the development and application of turbulent fluctuation metering equipment has made field measurements

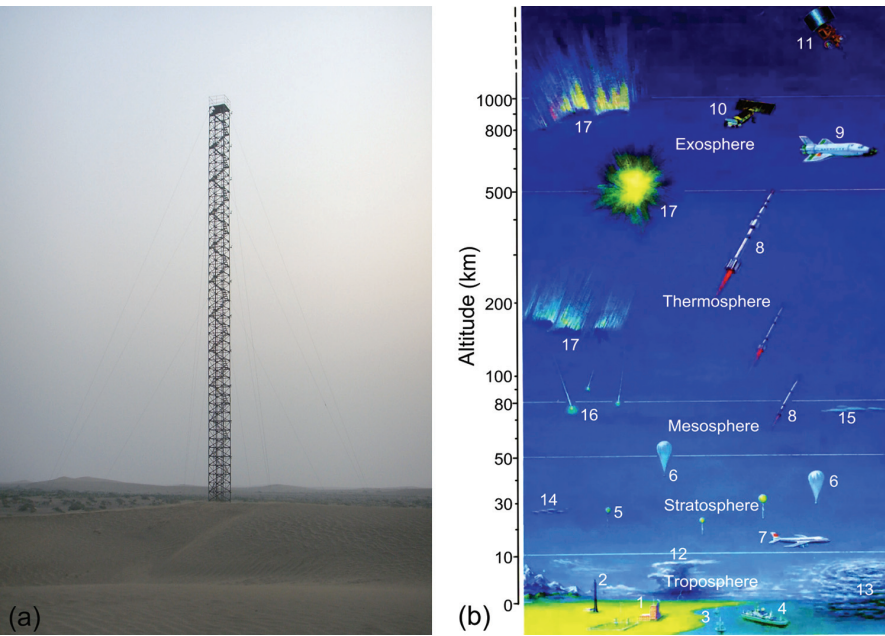


Fig. 2.2. Meteorological Observing System; **(a)** weather observation tower (photo by the author et al. in Minqin, China); **(b)** comprehensive meteorological measurement system, including: 1 weather observation stations, 2 meteorological tower, 3 buoy station, 4 marine weather ship, 5 sounding balloons, 6 high-altitude balloon, 7 weather aircraft, 8 meteorological rocket, 9 space shuttle, 10 polar orbit meteorological satellite, 11 geostationary meteorological satellite, 12 cumulonimbus, 13 typhoon, 14 nacreous clouds, 15 luminous cloud, 16 meteor, 17 Aurora (from Beijing geography teaching resources network)



Fig. 2.3. Released balloon (from Liu 2006)

become more and more sophisticated. The predominate physical processes taking place in the atmospheric boundary layer are exchanges and transports of momentum, energy, vapor and other materials due to turbulence. The exchange and transport processes determine the physical distribution and variance with time of physical quantities and the result is that the physical quantities will be transported from high-value area to low-value areas. Therefore, the subjects of interest in the observations of the boundary layer mainly include the following aspects: (1) the heat flux (such as latent heat flux, sensible heat flux): the heat arises from the solar radiation transported by turbulence from the ground to the boundary layer or from high temperature areas to low temperature areas; (2) the momentum flux: the momentum transferred from high wind power areas to low wind power areas, and mass of aerosol such as vapor and pollutants from high concentration area to low concentration area; and (3) fluctuating information of wind velocity and direction, correlation, flux and temporal and spatial distribution of the turbulence spectrum. This is required, on one hand, to reflect the strength of turbulence, and thus the intensity of turbulent transport, and on the other hand to describe the effect of frictional dissipation of the turbulence in the boundary layer on the atmospheric motion. The observations of those quantities mentioned above are primarily conducted 1.5 m above the human action space (see Fig. 2.2b, Fig. 2.4), while few results below 1 m are obtained.



Fig. 2.4. Tower measuring instruments including CSAT3 3-D Sonic Anemometer and LI7500 Open-gas Analyzer (from College of Atmospheric Sciences, Lanzhou University)

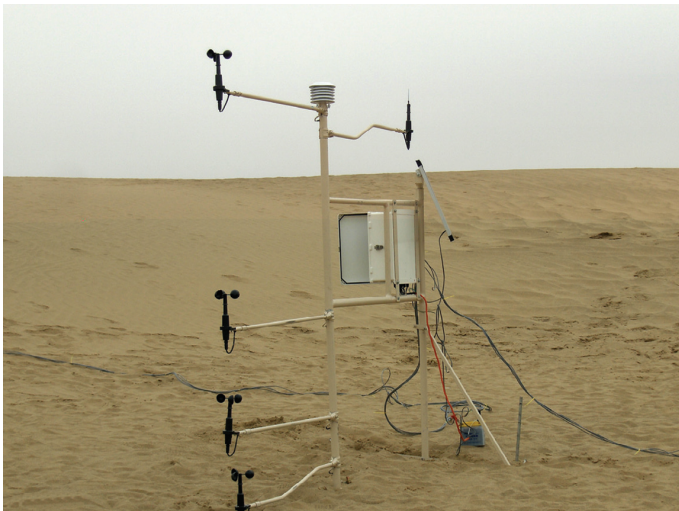


Fig. 2.5. The synchronization multipoint measurement system equipped with high sensitivity cup anemometer, which can be used to obtain the 1 Hz turbulence information of the near surface boundary flow (placed in Minqin, China by the author et al.)

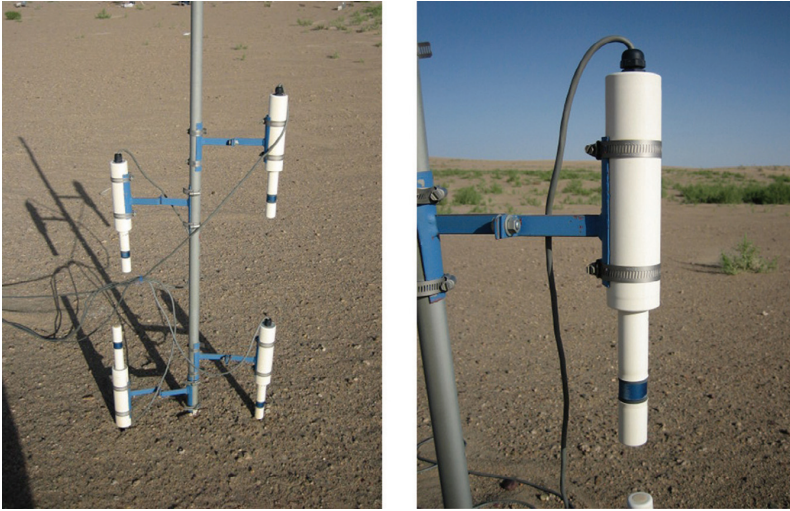


Fig. 2.6. The piezoelectric kinetic sensor for impact events measurement, with a frequency of 1 Hz which can be used to measure sand saltation activity (placed in Minqin, China by the author et al.)

The equipment for field observation usually includes a cup anemometer (uniaxial and triaxial paver), a propeller anemometer, an ultrasonic velocimeter, a unidirectional weathercock, and a bidirectional weathercock. Both the cup anemometer and the ultrasonic velocimeter can be equipped on a rod, support or multilayer elevated tower (see Fig. 2.4). Cup anemometers are more widely adopted in meteorological observation for their low cost, in spite of the fact that their measurable frequency is 1 Hz, the measurable wind velocity is not zero and its own inertia affects its precision. Ultrasonic velocimeters can discern a wind of nearly $0 \text{ m}\cdot\text{s}^{-1}$, have no inertia and their measurable frequency is up to 50 Hz (some even up to 100 Hz). Its precision is high enough to measure the ground surface turbulence. Fig. 2.5 shows a synchronized multipoint measurement system equipped with a high sensitivity cup anemometer to measure the ground surface wind-blown sand flux in Minqin, Gansu. Fig. 2.6 is the system's piezoelectric kinetic energy sensor, which is used to count impacts of sand particles. The output data represents the number of impacting particles during a time period which can indirectly reflect the intensity of wind-blown sand flux (Stout and Zobeck 1997).

A hot-wire (hot-film) anemometer is usually used to measure high frequency wind fluctuation. There are two types: the constant-flow type and the constant-temperature type. Before the 1950s, the constant-flow hot wire anemometer was widely employed to measure low turbulent flows.

However, after the 1950s, it has been gradually replaced by the constant-temperature hot-wire anemometer. The latter can be used to measure turbulent flows of diversified intensity with the following advantages: (1) small volume and little disturbance to the flow field; (2) capability of measuring high frequency fluctuating velocities of turbulence; (3) simultaneous measuring of velocity components in multiple directions; (4) high response frequency (up to 1 MHz). The disadvantages of the constant-temperature hot wire anemometer include: (1) the sensor is susceptible to damage during the experiment; (2) incapable of measuring reverse flow; (3) calibrations required before measuring.

In the last twenty years, hot wire (film) anemometer has been widely used in the turbulent measurement of wind-blown sand dynamics for its ability to measure the characteristics of flow inside the wind-blown sand flux (below 5 cm). For example, Butterfield (1991) measured the wind velocity of the windblown sand flux 2 cm above the ground with a hot-wire meter with stainless thimbles. However, most commercial probes or sensors are susceptible to damage by the sand and wind, unless a shield is used, though this interferes with the measurement of frequency reducing it to below 10 Hz.

In the laboratory, a wind tunnel is used to drive a controllable piped air flow over a static mould or sand bed to measure the aerodynamical force acting on the mould or the flow near the sand bed. Based on the similarity theory, experimental data statistics can be converted into dimensionless coefficients for the corresponding practical object. In a wind tunnel experiment, it requires not only that model should be in a similar mode as the practical application, but also that these parameters of the flow field should be the same as the practical ones. These parameters are dimensionless resultant quantities derived from several parameters, which can be deduced from the basic dimensionless equations, to ensure the similarity. However, in practice, due to the limitation of the size and drive force of the wind tunnel, only the major similarity criteria such as the Reynolds number and Mach number can be satisfied. The experimental section is in the central part of the wind tunnel, where the mould is placed. Therefore, the quality of air flow, such as uniformity, stability and intensity of turbulence, should meet a certain standard. The advantage of a wind tunnel lies in the fact that the experimental conditions, including the air flow and mould state, are easily controlled; individual parameters can be changed independently; the experiment is not affected by the atmospheric environment; the experimental period is short and the cost is relatively low. But it also has disadvantages, such as the inability to meet all similarity principles and the susceptibility to air flow boundaries. As far as wind-blown sand movement is concerned, a low-speed (less than $100 \text{ m}\cdot\text{s}^{-1}$) blow down wind tunnel as

shown in Fig. 2.7 is required. This kind of wind tunnel can measure the lift-off velocities of sand particles, the saltation activity of the wind-blown sand flux, the evolution of aeolian landforms, the validity of sand breaking measures, the intensity of wind-blown sand electric fields and the degree of wind erosion.

Flow fields in the wind tunnel are usually measured by pitot tube, hot wire (film) anemometer, laser doppler velocimeter, phase doppler anemometer (PDA) and particle image velocity (PIV). Among these, PIV developed from the speckle methods in solid mechanics in 1970s and can be used for measuring turbulent fluctuations with high precision. As a piece of non-contact optical equipment, it can provide comprehensive instantaneous information about unsteady flow without disturbing the flow field.



Fig. 2.7. Low-speed blow down wind tunnel (Multi-function environmental wind tunnel of Lanzhou University), which contains four sections: the power part, the rectifier part, the experimental part and the proliferation part. The total length of the wind tunnel is 85 m, the experimental section is up to 20 m, the cross-sectional area is about 1.3 m (width) \times 1.45 m (height), wind velocity is adjustable from $4 \text{ m}\cdot\text{s}^{-1}$ to $40 \text{ m}\cdot\text{s}^{-1}$

2.5 Basic Equations of the Atmospheric Boundary Layer

In this section, we first introduces the basic equations of flows in the atmospheric boundary layer, which are the specific forms stemming from the equations introduced in Sect. 2.2 for atmospheric motions, then the concept of aerodynamic roughness and finally the influence of sand saltation and sand dunes on the flow field are given.

2.5.1 Basic Equations

Based on the Boussinesq assumption (Haugen 1973), the pressure, density and temperature of the fluid can be expressed as $P = P_0 + p$, $\rho = \rho_0 + \rho'$ and $T = T_0 + T_d$ respectively, it is known that the gradient of T_0 and P_0 , can be expressed as $\partial T_0 / \partial x_3 = -g/c_p = -\gamma_d$ and $\partial P_0 / \partial x_3 = -g\rho_0$ in direction x_3 respectively. Compared to the static atmosphere (P_0 , ρ_0 , T_0), variation of thermodynamic quantities (p , ρ' , T_d) caused by the flow is very little. Furthermore, besides gravity, pressure gradient force and viscous force, Coriolis force $2\Omega(\boldsymbol{\eta} \times \mathbf{u})$ caused by the Earth's rotation also acts on the atmosphere boundary layer, so the body force in the basic equations of incompressible flow (see Eqs. 2.7 and 2.11) is now the sum of gravity and the Coriolis force, with $\boldsymbol{\eta}$ is unit vector which parallels the Earth axis of rotation; Ω is the Earth's angular velocity of rotation. Neglecting the variation of heat energy caused by atmospheric radiation and molecular viscous dissipation, the equations for the atmospheric boundary layer can be written as:

$$\text{continuity equation} \quad \frac{\partial u_i}{\partial x_i} = 0, \quad (2.16)$$

$$\text{momentum equation} \quad \frac{\partial u_i}{\partial t} + u_j \frac{\partial u_i}{\partial x_j} = -\frac{1}{\rho} \frac{\partial P}{\partial x_i} - g\delta_{3i} + \nu \frac{\partial^2 u_i}{\partial x_j^2} - 2\Omega \varepsilon_{ijk} \eta_j u_k, \quad (2.17)$$

$$\text{heat energy equation} \quad \frac{\partial T}{\partial t} + u_j \frac{\partial T}{\partial x_j} = -\frac{g}{c_p} + k_T \frac{\partial^2 T}{\partial x_j^2}, \quad (2.18)$$

$$\text{and state equation} \quad P = \rho RT, \quad (2.19)$$

where $k_T = \lambda_T / \rho c_p$ is thermal diffusivity.

According to atmosphere boundary theory (see Haugen 1973), the Coriolis force in the surface layer below 20–80 m can be neglected. In this

manner, the equations of atmospheric flow in the surface layer can be obtained through equations of the atmospheric boundary layer (i.e., Eqs. 2.16–2.19). Using the Boussinesq assumption that ν and k_T are constants and the flow is incompressible, the heat energy equation can be simplified to $\rho'/\rho_0 = -T_d/T_0$. For the sake of convenience, the equations of atmospheric flow are expressed with components (u, v, w) of velocity vector (\mathbf{u}) under the Cartesian coordinate system $Oxyz$.

$$\frac{\partial u}{\partial x} + \frac{\partial v}{\partial y} + \frac{\partial w}{\partial z} = 0, \quad (2.20)$$

$$\frac{\partial u}{\partial t} + u \frac{\partial u}{\partial x} + v \frac{\partial u}{\partial y} + w \frac{\partial u}{\partial z} = -\frac{1}{\rho_0} \frac{\partial p}{\partial x} + \nu \left(\frac{\partial^2 u}{\partial x^2} + \frac{\partial^2 u}{\partial y^2} + \frac{\partial^2 u}{\partial z^2} \right), \quad (2.21a)$$

$$\frac{\partial v}{\partial t} + u \frac{\partial v}{\partial x} + v \frac{\partial v}{\partial y} + w \frac{\partial v}{\partial z} = -\frac{1}{\rho_0} \frac{\partial p}{\partial y} + \nu \left(\frac{\partial^2 v}{\partial x^2} + \frac{\partial^2 v}{\partial y^2} + \frac{\partial^2 v}{\partial z^2} \right), \quad (2.21b)$$

$$\frac{\partial w}{\partial t} + u \frac{\partial w}{\partial x} + v \frac{\partial w}{\partial y} + w \frac{\partial w}{\partial z} = -\frac{1}{\rho_0} \frac{\partial p}{\partial z} + g \frac{T_d}{T_0} + \nu \left(\frac{\partial^2 w}{\partial x^2} + \frac{\partial^2 w}{\partial y^2} + \frac{\partial^2 w}{\partial z^2} \right), \quad (2.21c)$$

$$\frac{\partial T_d}{\partial t} + u \frac{\partial T_d}{\partial x} + v \frac{\partial T_d}{\partial y} + w \frac{\partial T_d}{\partial z} = k_T \left(\frac{\partial^2 T_d}{\partial x^2} + \frac{\partial^2 T_d}{\partial y^2} + \frac{\partial^2 T_d}{\partial z^2} \right), \quad (2.22)$$

$$\frac{\rho'}{\rho_0} = -\frac{T_d}{T_0}. \quad (2.23)$$

Considering the neutral situation (i.e., the gradient Richardson number, R_i , is close to zero), and the viscous term is two orders smaller than the corresponding turbulence term and thus can be neglected at the height more than 10 cm above the ground surface (Haugen 1973), the equations can be simplified by applying the Reynolds averaged treatment to Eqs. 2.20–2.21 as

$$\frac{\partial \bar{u}}{\partial x} + \frac{\partial \bar{v}}{\partial y} + \frac{\partial \bar{w}}{\partial z} = 0, \quad (2.24)$$

$$\frac{\partial \bar{u}}{\partial t} + \bar{u} \frac{\partial \bar{u}}{\partial x} + \bar{v} \frac{\partial \bar{u}}{\partial y} + \bar{w} \frac{\partial \bar{u}}{\partial z} = -\frac{1}{\rho_0} \frac{\partial \bar{p}}{\partial x} - \frac{1}{\rho_0} \left(\rho_0 \frac{\partial \overline{u'^2}}{\partial x} + \rho_0 \frac{\partial \overline{u'v'}}{\partial y} + \rho_0 \frac{\partial \overline{u'w'}}{\partial z} \right), \quad (2.25a)$$

$$\frac{\partial \bar{v}}{\partial t} + \bar{u} \frac{\partial \bar{v}}{\partial x} + \bar{v} \frac{\partial \bar{v}}{\partial y} + \bar{w} \frac{\partial \bar{v}}{\partial z} = -\frac{1}{\rho_0} \frac{\partial \bar{p}}{\partial y} - \frac{1}{\rho_0} \left(\rho_0 \frac{\partial \overline{u'v'}}{\partial x} + \rho_0 \frac{\partial \overline{v'^2}}{\partial y} + \rho_0 \frac{\partial \overline{v'w'}}{\partial z} \right), \quad (2.25b)$$

$$\frac{\partial \bar{w}}{\partial t} + \bar{u} \frac{\partial \bar{w}}{\partial x} + \bar{v} \frac{\partial \bar{w}}{\partial y} + \bar{w} \frac{\partial \bar{w}}{\partial z} = -\frac{1}{\rho_0} \frac{\partial \bar{p}}{\partial z} - \frac{1}{\rho_0} \left(\rho_0 \frac{\partial \overline{u'w'}}{\partial x} + \rho_0 \frac{\partial \overline{v'w'}}{\partial y} + \rho_0 \frac{\partial \overline{w'^2}}{\partial z} \right). \quad (2.25c)$$

It can be seen that the Reynolds averaged equations of the flow are not closed. Therefore, any of the turbulence models mentioned in Sect. 2.2.5 can be involved to make them closed so as to solve them analytically or numerically.

Supposing that x is in the direction of the mean horizontal velocity and z the mean vertical velocity, on a homogeneous ground of even roughness, since the pressure gradient force and the molecular viscous force are of the same order, the two forces can be neglected. So the Eqs. 2.25 can be simplified to

$$\frac{\partial \bar{u}}{\partial t} = \frac{1}{\rho_0} \frac{\partial}{\partial z} (-\rho_0 \overline{u'w'}), \quad 0 = \frac{1}{\rho_0} \frac{\partial}{\partial z} (-\rho_0 \overline{v'w'}), \quad 0 = \frac{1}{\rho_0} \frac{\partial}{\partial z} (-\rho_0 \overline{w'^2}). \quad (2.26)$$

In a steady situation, the Eq. 2.26 can be simplified to

$$\frac{\partial}{\partial z} (-\rho_0 \overline{u'w'}) = \frac{\partial \tau}{\partial z} = 0, \quad (2.27)$$

where $\tau = -\rho_0 \overline{u'w'}$ is the turbulence shear stress. According to Prandtl's mixing length theory, $\tau = \mu_t \partial \bar{u} / \partial z$, $\mu_t = \rho_0 l_m^2 |\partial \bar{u} / \partial z|$, and the mixing length l_m is in direct proportion to the distance from the wall. That is, $l_m = kz$, where $k=0.4$ is Karman constant. Then $\tau = \rho_0 k^2 z^2 (\partial \bar{u} / \partial z)^2$, and the following equation can be inferred from Eq. 2.27.

$$\tau = \rho_0 k^2 z^2 \left(\frac{\partial \bar{u}}{\partial z} \right)^2 = \tau_0. \quad (2.28)$$

where τ_0 is the friction stress of the surface. If $u_{*0} = \sqrt{\tau_0 / \rho_0}$ is defined as the surface friction velocity and substituted into the above equation, then

$$\frac{\partial \bar{u}}{\partial z} = \frac{u_{*0}}{kz}. \quad (2.29)$$

After integration of the above equation, the logarithmic velocity profile is

$$\bar{u} = \frac{u_{*0}}{k} \ln \frac{z}{z_0} \quad \text{or} \quad u = 5.75 u_{*0} \lg \frac{z}{z_0}, \quad (2.30)$$

where z_0 is usually called the aerodynamic roughness, and should be determined through experiments.

Since Eq. 2.27 is applicable within the layer ranging from 10 cm to 20–80 m above the ground surface, the friction velocity u_* in this layer equals to the surface friction velocity u_{*0} . In our following discussion, we will use u_* instead of u_{*0} . In addition, in the neutral situation, we can further use ρ to replace ρ_0 and neglect the small variation of air density.

2.5.2 Aerodynamic Roughness

Aerodynamic roughness z_0 indicates the abated effect of the ground surface on the wind velocity at a certain height above the ground where wind velocity is zero. It is an important parameter in the parameterization of fluid mechanics and atmospheric boundary layer turbulent characteristics. Different landforms have different influences on the fluid flow over them. Roughness of the ground surface changes not only the flow velocity gradient but also its range, and thus forms boundary layer flow with various properties. Therefore, a correct understanding and description of aerodynamic roughness is helpful to model and predict fluid movement.

Since the complex land surface causes local imbalance in air current, roughness is divided into the effective roughness and the local roughness. The effective roughness is the large scale aerodynamic roughness and corresponds to the total ground surface stress, i.e., total momentum flux, while local roughness is the small scale aerodynamic roughness and corresponds to local ground surface stress. According to the properties of the fluid flow over the ground, roughness is divided into isotropic roughness and anisotropic roughness and the latter is the reason for the eddy turbulence. A roughness element is the smallest unit producing surface roughness and a crucial element of ground roughness. Its type, size, shape, arrangement and movement all exert influence on ground roughness. In terms of type, there are sandy roughness, snowy roughness, watery roughness, gravel roughness and vegetation roughness, and in terms of movement type, there are fixed bed roughness, transitional type roughness (water surface roughness) and movable bed roughness. Movable bed roughness is related to the particle size distribution and movement. Since roughness z_0 is closely related to the threshold friction velocity u_{*t} (Greeley

and Iversen 1985), z_0 also affects the absolute and relative sediment discharge. Therefore, aerodynamic roughness plays a crucial role in the wind-blown sand transport, and migration of sand dunes and the evolution of the Gobi deflation planes.

There are four methods to obtain aerodynamic roughness: logarithmic profile fitting method, mass conservation method, center of pressure method and resistance method. The first method is the most used in practice under the prerequisite that the wind velocity obeys a logarithmic law. Through fitting all results of Eq. 2.30 for wind velocity measured at three or more than three heights with the least square method, the roughness z_0 can be obtained. However, in reality, the wind profile close to the surface only roughly satisfies logarithmic law, as is shown in Sect. 2.5.1. Therefore, it's reasonable to seek the roughness in the view of the air turbulent structure. More and more relevant studies are available and interested readers may consult Raupach et al. (1991).

2.5.3 Characteristics of the Flow Field on the Wind-Blown Sand Boundary Layer

For the near surface layer (less than 2 m), the turbulence is mainly influenced by the horizontal wind shear and frictional resistance of the rough surface. Since the velocity profile is little affected by the thermal turbulence, it can be expressed approximately with the logarithmic wind profile (see Eq. 2.30). However, due to the wind force, a saltation layer will be formed above the sandy surface. The density of sand particles is not uniform in the saltation layer but decreases drastically as the height increases. Generally speaking, the saltation height is no more than 0.5 m and thus the saltation layer is very thin compared with the surface layer. Those moving sand particles will in turn exert an effect on the wind velocity, which is actually the reaction force of sand particles on the flow field according to Newton's Third Law. The force acting on the wind per volume is denoted as $F_x(z)$. In Eq. 2.26, taking the effect of $F_x(z)$ into consideration while neglecting the influence of viscosity, the flow equation of air in the saltation layer in the case of a flat and homogeneous surface can be obtained,

$$\rho_0 \frac{\partial \bar{u}}{\partial t} = \frac{\partial \tau_a}{\partial z} + F_x(z), \quad (2.31)$$

where $\tau_a = \rho u_{*a}^2$ is the turbulence shear stress. According to Prandtl's mixing length theory, it can be rewritten as

$$\rho_0 \frac{\partial \bar{u}}{\partial t} = \frac{\partial}{\partial z} \left[\rho_0 k^2 z^2 \left(\frac{\partial \bar{u}}{\partial z} \right)^2 \right] + F_x(z). \quad (2.32)$$

In the steady situation, the above equation can be expressed as

$$\frac{\partial \tau_a}{\partial z} + F_x(z) = 0. \quad (2.33)$$

If the vertical momentum flux τ_s produced by sand movement in the thin layer $[z - dz/2, z + dz/2]$ at the height z is considered, it can be seen that

$$F_x(z) = \frac{\partial \tau_s}{\partial z}. \quad (2.34)$$

At the upper boundary of the saltation layer, the turbulence shear stress is determined by the outer flow field, and is generally taken as τ_0 . It can be inferred from Eqs. 2.33 and 2.34 that $\tau_a + \tau_s = \tau_0$, so

$$\frac{\partial \bar{u}}{\partial z} = A \frac{u_{*a}}{z} = \frac{1}{kz} \sqrt{\frac{\tau_0 - \tau_s}{\rho}}. \quad (2.35)$$

According to the contribution of the Sauermann et al. (2001), the above equation can be adapted into

$$\frac{\partial \bar{u}}{\partial z} = A \frac{u_{*a}}{z} = \frac{u_{*0}}{kz} \sqrt{1 - \frac{\tau_{s0}}{\tau_0} \exp\left(-\frac{z}{H_s}\right)}, \quad (2.36)$$

where H_s is the thickness of mean saltation. If the value of z_0 is properly attained, the continuity of the flow field's velocity outside the saltation layer can be assured. In addition, the analytic expression of the velocity in the wind-blown sand flux was also given by Raupach (1991).

Since the transport of sand particles and the turbulent fluctuation near the surface are both mainly horizontal (for the latter, the horizontal fluctuation is about 10 times larger than the vertical fluctuation), the turbulent stress in the saltation layer must be greatly reduced by the resistance of moving sand particles on the turbulent fluctuation, but the turbulent stress outside the saltation layer is unaffected. However, since the turbulent stress changes the velocity gradient, the velocity of the air flow outside the saltation layer will also be reduced. Owen (1964) considered the influences of the saltation layer and the ground friction as equal to another ground roughness and calculated wind profile outside the saltation layer using this train of thought. Owen (1964) believed that the wind profiles outside the saltation layer also obeys the logarithmic distribution on the condition that

the aerodynamic roughness z_0 is changed into equivalent roughness or movable bed roughness z_s , which is a physical quantity in wind-blown sand physics as important as the aerodynamic roughness.

2.5.4 Effect of Sand Dunes on the Flow Field

Erosion and deposit caused by wind erosion will change the landforms and give birth to complicated geomorphological patterns, such as sand dunes, sand ridges and sand ripples. When it flows over these complex landforms, the air flow will also become complicated under the influence of the landforms. In the following part, a simple case of changes in the flow field when the air flow perpendicularly passes an isolated traverse dune is studied.

According to the theory of Hunt, Leibovich and Richards (HLR) (Hunt et al. 1988), the flow field is divided into the inviscid outer region and the thin inner region. The average velocity in the latter still meets the wall law, while the velocity variance in the former is caused by pressure fluctuation. The two flow layers can further be divided into two sub-layers, respectively as shown in the Fig. 2.8.

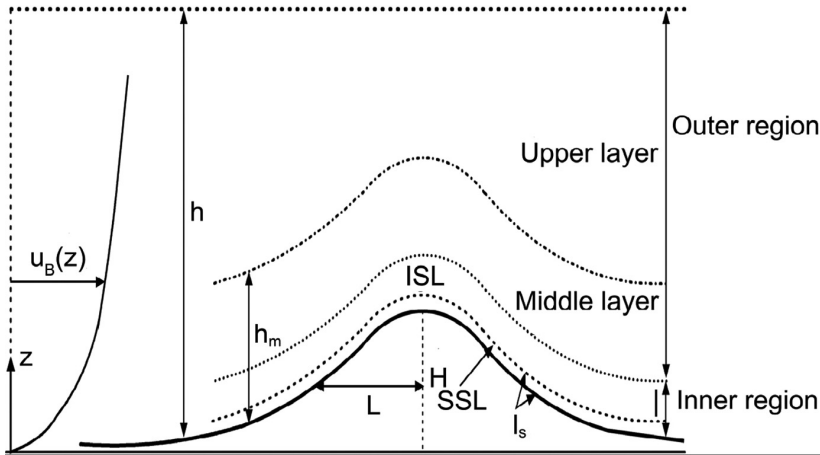


Fig. 2.8. Division of the flow field passing a two-dimensional terrain: upper layer, mid-layer, inner surface layer (ISL) and shear surface layer (SSL), where H is the terrain height, L is the horizontal distance from the top of the sand dune to the mid-point of the windward slope, the terrain surface shape is $z = h_{dune}(x)$, u_B is the flow velocity corresponding to h_m , which is the height of the mid-layer, besides, the surface roughness z_0 is a constant

According to the HLR theory, the inner layer depth l_{inner} which can be calculated from $l_{inner} = 2k^2L / \ln(l_{inner}/z_0)$, is usually much higher than the saltation layer. The velocity profile in this layer follows logarithmic law, while the friction velocity u_* is not equal to the inflow friction velocity u_{*0} , but substituted by another value with taking into account of the local disturbance instead. According to HLR's assumption, the disturbance of the friction stress is linear, so it follows the following equation

$$\tau(x) = \tau_0 (1 + \hat{\tau}(x)). \quad (2.37)$$

Based on the friction stress expression of Weng et al. (1991), Sauermann et al. (2001) made a simplification of $\hat{\tau}(x)$ which can be expressed as

$$\hat{\tau}(x) = A \left(\frac{1}{\pi} \int_{-\infty}^{\infty} \frac{\dot{h}_{dune}}{x - \xi} d\xi + B \dot{h}_{dune} \right), \quad (2.38)$$

where $A \approx 3.2$, $B \approx 0.25$.

Except for the HLR theory, it is also feasible method to determine velocity variation on the dune slope through experiments. From field observations and wind tunnel experiments, Mulligan (1988) and Lancaster et al. (1996) found that the shear velocity u_* is in a linear relation with the height from the bed,

$$u_* = u_{*-\infty} + k_* h_{dune}, \quad (2.39)$$

where h_{dune} is the height from the bed, $u_{*-\infty} = u_{*0}$ is the friction velocity of the inflow at the infinite distance, k_* is the velocity increment which is related to the dune height H . Because the shear velocity u_* is in a linear relation to the height h_{dune} , the velocity acceleration factor α_{dune} ($= u_{*crest}/u_{*-\infty}$), u_{*crest} is the wind velocity on the dune top) can be used to describe the evolution of the wind velocity acceleration on the windward slope of the dune. According to the relationship between the wind velocity acceleration factor α_{dune} and the angle of the windward slope (Lancaster 1985) and the relationship between the angle and the dune height, the following expression can be obtained

$$k_* = \frac{(\alpha_{dune} - 1)u_{*-\infty}}{H} = \frac{u_{*-\infty}}{H} \left[\alpha_0 - 1 + 2k_1 \tan \left(A + \ln \frac{H - B}{C} \right) \right], \quad (2.40)$$

where A , B , C , α_0 and k_1 are empirical parameters varying for different regions, which should be determined by observations and measurements conducted in the regions concerned.

Because of flow separation, an eddy current is usually formed on the leeward slope. The downwind velocity may decrease quickly to zero and even become negative. When the along-wind velocity is at an angle with the transverse dune, secondary flow along the dune will appear. The studies of Walker and Nickling (2002) showed that secondary flow is the reason for the appearance of sand ripples on the leeward side of sand dunes.

2.6 Wind Gusts near the Earth's Surface

Here wind gusts represent the wind fluctuations near the surface which are not the same as the definition of Cheng et al. (2007). Wind gusts affect the transfer of momentum, heat and material there. Their effects are embodied not only in the transmission of momentum through the Reynolds stress which makes erosion and deposition occur, but also in making the erosion process unstable and intermittent because of large turbulent intensity. Although wind gusts play an important role in the transport of particles from an erodible surface, most previous researches focused on steady state sediment transport, which means that both turbulence stress and wind velocity are time-averaged. In this case, although more and more factors (various aerodynamic forces exerted on a sand particle, the effects of particle size, particle shape, moisture level, heterogeneous saltation, collisions between particles in air, etc.) are taken into account in the prediction models, the simulated mass-flux relations show only moderate mutual agreement. According to the results of Anderson and Haff (1991), the responding time of mass flux to wind variations is no less than one second, so the wind fluctuations in this time scale should be considered in detail.

So the research of erosion processes should include wind gusts rather than mere steady flow (Zeng et al. 2007). The effects of wind gusts can be seen from the measured results of wind velocity and dust entrainment in a dust storm in Beijing, shown in Fig. 2.9 (Zeng et al. 2006).

It is known that the atmospheric turbulence spectrum contains three independent regions: the weather-scale region, the spectrum window and the turbulence scale region, and two peaks: one appears at a rate of 10^{-2} per hour, which belongs to weather scale, the other appears at 50 per hour. The latter results from turbulence fluctuations which can be affected by surface friction and dynamical interactions of turbulence eddies or thermal instability, so it belongs to the turbulence scale region. The near surface wind gusts, which show evident turbulent characteristics (instability, randomness, multi-scale characteristics, and intermittency), are contained in the second scale (see Kaimal et al. 1972).

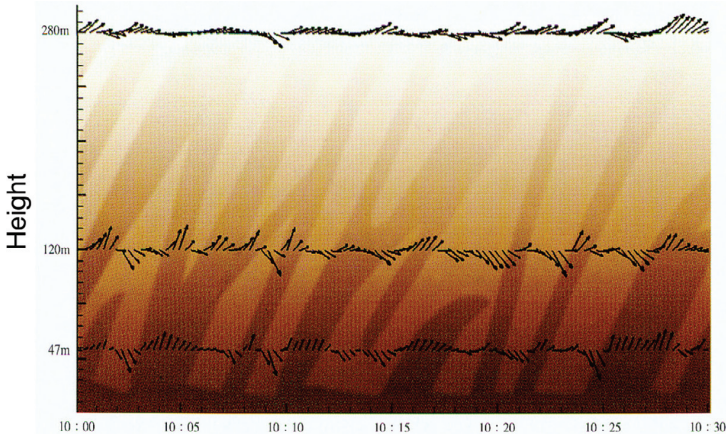


Fig. 2.9. Variations of the velocity vector and the concentration of dust with time, the data has been smoothed by 1 minutes interval (from Zeng et al. 2006)

In the following discussion, wind velocity and saltation activity measured at different heights from bare ground and dune crest are given out. It is found through calculating the correlation dimensions of the experimental data that both the wind gusts and the sand transport variations should be regarded as a dominant random behavior rather than chaos. Based on an analysis of the stochastic characteristics of the sand flux and turbulence, we discover that the sand transport is a highly intermittent process and may be mainly correlated with wind gusts in a time scale of about 3 min. Finally, a wind prediction model which can be used to define the wind velocity variations with time and height is proposed according to the characteristic analysis of the near-surface wind turbulence.

2.6.1 Analysis of the Wind Gusts

Experiments were performed to measure the wind profile (and sand transport flux) on bare inter-dunes and a 8 m high sand dune crest on the edge of the Badain Jaran desert and the Tengger Desert in Minqin, China. Using fast response instruments (a lightweight fast-responding cup anemometer, a micro wind vane and a piezoelectric saltation sensor (Sensit), CR-3000 Micrologger, all of which were sampled at a rate of 1 Hz, shown in Figs. 2.5 and 2.6), continuous and synchronous measurements of turbulent velocity fluctuations, wind direction and saltation activity at several heights were made. Figs. 2.10–2.12 show the variations of wind velocity with time for different time scales, from which it can be seen that even in one second scale the velocity still changes violently.

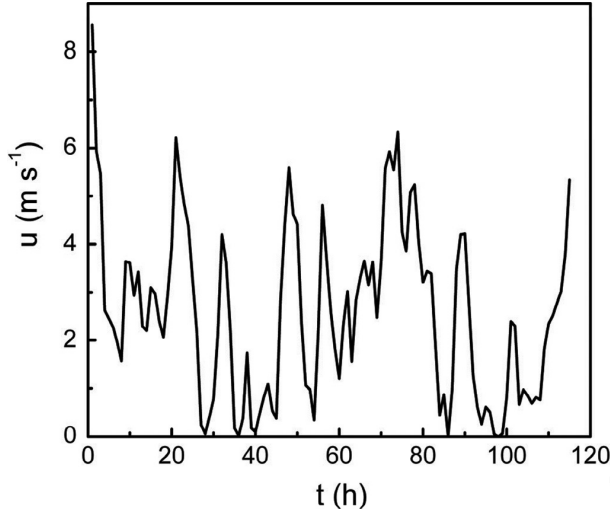


Fig. 2.10. The variations of wind velocity for the time scale of 1 hour at 2 m (measured by the author et al. on a flat ground in Minqin, China, during the period from October 28 to November 2, 2007)

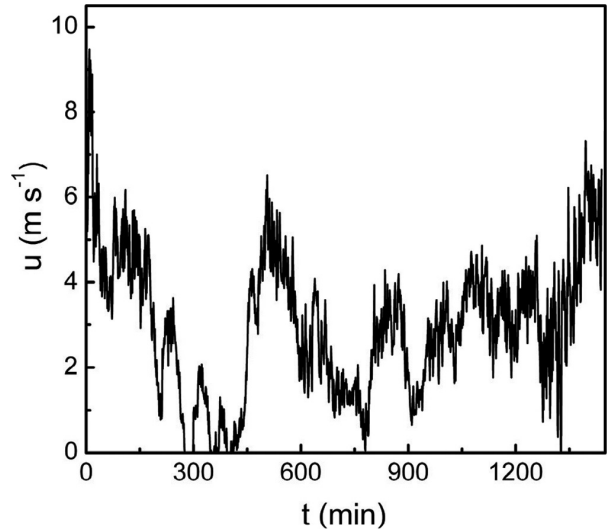


Fig. 2.11. The variations of wind velocity for the time scale of 1 min at 2 m (measured by the author et al. on flat ground in Minqin, China, during the period from October 28 to November 2, 2007)

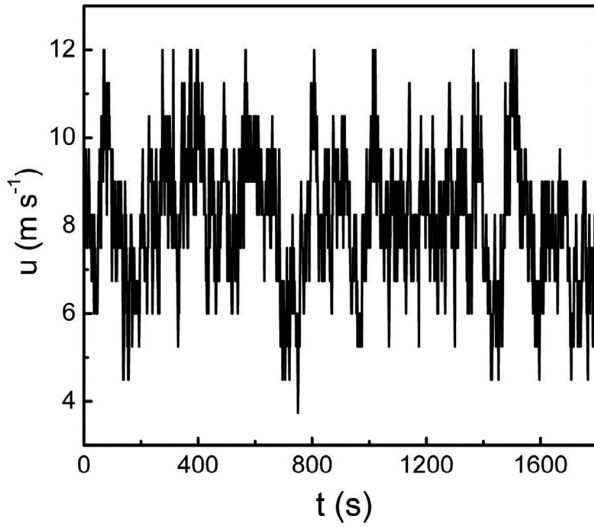


Fig. 2.12. The variations of wind velocity for the time scale of 1 second at 2 m. (measured by the author et al. on flat ground in Minqin, China, during the period from October 28 to November 2, 2007)

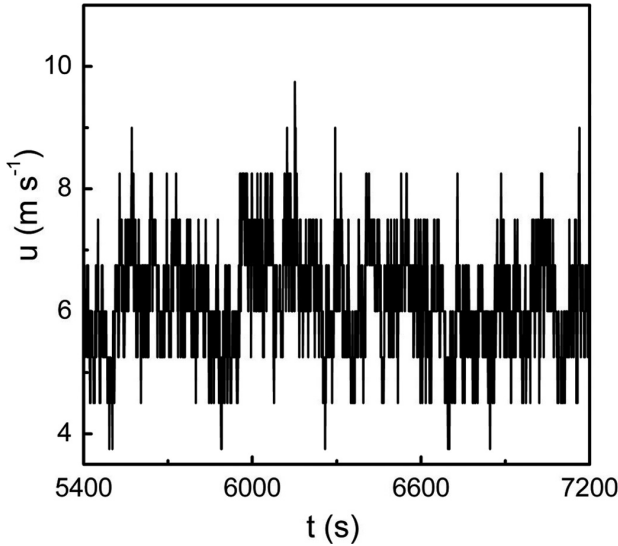


Fig. 2.13. The wind velocity at height of 0.15 m (measured by the author et al. on a dune crest in Minqin, China during the period from October 27 to October 28, 2007 with equipment shown in Fig. 2.5 and Fig. 2.6)

The wind velocity, wind direction and saltation activity on the dune crest were measured over a 2 hours period, part of the experimental results are presented in Figs. 2.13–2.15, which reveals evident fluctuations of the sediment transport flux as well as the flow velocity.

In order to analyze the nature of the random experimental signal, i.e., to see whether it belongs to a chaotic system or is just stochastic, the correlation dimension of the wind velocity and the saltation activity data are calculated. The experimental data are time series, which can be denoted by $\{x(t_i), t_i = t_0 + i\Delta t\}$, where $\Delta t = 1$ s, and $x(t_i)$ represents the physical quantity measured at t_i , such as wind velocity, saltation activity, etc. Before the calculation, an m -dimensional phase space should be formed from $x(t_i)$, which can be represented by $\{\mathbf{X}_i, i = 1, 2, \dots, m\}$, where \mathbf{X}_i is a point in an m -dimensional phase space, which can be denoted as:

$$\mathbf{X}_i = (x_i, x_{i+\Delta\tau}, x_{i+2\Delta\tau}, \dots, x_{i+(m-1)\Delta\tau}) \quad i = 1, 2, \dots, N_0, \quad (2.41)$$

where $N_0 = N - (m-1)\Delta\tau$, $\Delta\tau$ is delay time lag and N is the total data number. Then, the correlation dimension of $x(t_i)$ can be defined in the following way:

$$d_c(m) = \lim_{\varepsilon_d \rightarrow 0} \frac{\ln C(\varepsilon_d, m)}{\ln \varepsilon_d}, \text{ while } C(\varepsilon_d) = \frac{N(i, j)}{N_0(N_0 - 1)}, \quad (2.42)$$

where $N(i, j)$ is the number of the pairs $(\mathbf{X}_i, \mathbf{X}_j)$ which satisfies $\|\mathbf{X}_i - \mathbf{X}_j\| < \varepsilon_d$. So we have:

$$C(\varepsilon_d, m) = \frac{1}{N_0(N_0 - 1)} \sum_{i=1, j=0, i \neq j}^{N_0} s(\varepsilon_d - \|\mathbf{X}_i - \mathbf{X}_j\|), \quad (2.43)$$

where $s(z)$ is Heaviside step function, and is expressed as

$$s(z) = \begin{cases} 0, & \text{if } z < 0 \\ 1, & \text{if } z \geq 0 \end{cases}. \quad (2.44)$$

If there exists a m_0 making $d_c(m)$ ($m \geq m_0$) approach a fixed value when $\varepsilon_d \rightarrow 0$, namely,

$$d_c(m_0) = d_c(m_0 + 1) = d_c(m_0 + 2) = \dots = d_c. \quad (2.45)$$

We can conclude that the mechanical system which produces the experimental data exhibits the characteristics of chaos. If the above condition is not satisfied, the system is dominated by stochastic features (see Grassberger and Procaccia 1983). Because of the multi-scale characteristic of the wind turbulence, the experiment data are decomposed to multi-scales by the discrete wavelet transform method.

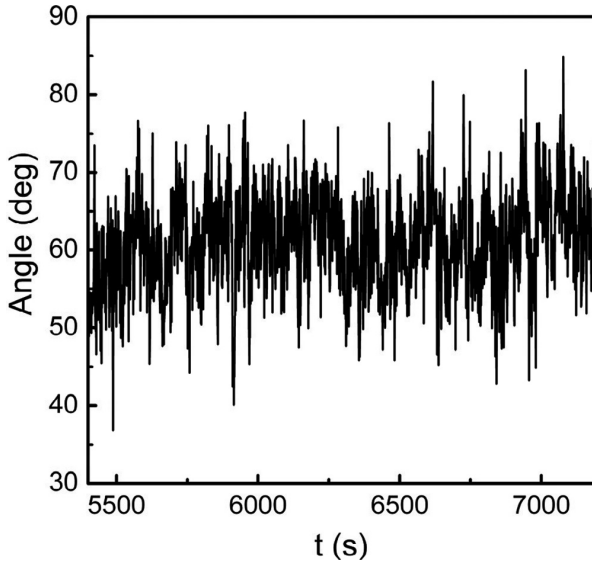


Fig. 2.14. Wind direction data at height of 2.0 m (measured by the author et al. on a dune crest in Minqin, China during the period from October 27 to October 28 in 2007 with equipment shown in Fig. 2.5 and Fig. 2.6)

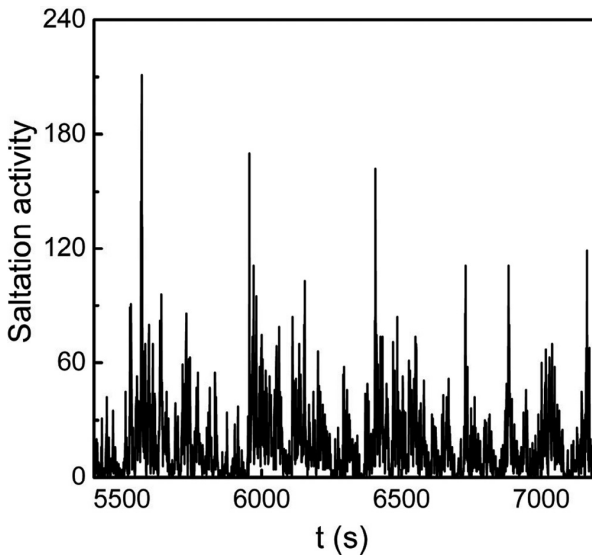


Fig. 2.15. Saltation activity at height of 0.04 m (measured by the author et al. on a dune crest in Minqin, China during the period from October 27 to October 28 in 2007 with equipment shown in Fig. 2.5 and Fig. 2.6)

Based on the wavelet theory, a signal $f(x)$ which belongs to real-space $L^2(R)$ can always be decomposed as the sum of a low-resolution part and several high-resolution parts in order to analyze the multi-scale characteristics. Suppose the scaling function is taken as the Daubechies scaling function $\phi(x)$, for example, which satisfies the following so-called ‘two-scale equation’,

$$\phi(x) = \sum_k p_k \phi(2x - k), \quad (2.46)$$

where $\{p_k\}$ is called the two-scale sequence for the scaling function. Corresponding to $\phi(x)$, the wavelet function $\psi(x)$ also satisfies its two-scale equation

$$\psi(x) = \sum_k q_k \phi(2x - k). \quad (2.47)$$

$\{q_k\}$ is called the two-scale sequence for the wavelet function. $\{p_k\}$ and $\{q_k\}$ are also called the low pass filter coefficient and the band-pass filter coefficient, respectively. If ‘expansion’ and ‘translation’ are performed to the scaling function and the wavelet function, the new functions can be defined by:

$$\begin{cases} \phi_{j,k}(x) = 2^{-j/2} \phi(2^{-j}x - k) \\ \psi_{j,k}(x) = 2^{-j/2} \psi(2^{-j}x - k) \end{cases} \quad j, k \in N. \quad (2.48)$$

Then for a given integer j , the functions sequences $\{\phi_{j,k}(x), k \in N\}$ and $\{\psi_{j,k}(x), k \in N\}$ can form two groups of linear subspace of $L^2(R)$, which can be expressed as:

$$\begin{cases} V_j = \text{span}\{\phi_{j,k}(x), k \in N\} \\ W_j = \text{span}\{\psi_{j,k}(x), k \in N\} \end{cases}. \quad (2.49)$$

These subspaces meet the nested relations: $\forall V_0 \subset V_1 \subset \dots \subset V_j \subset \dots \subset L^2(R)$, and $V_{j+1} = V_j + W_j$, so the function $f(x) \in L^2(R)$ can be decomposed as:

$$f^{j+1} = \sum_k c_k^{j+1} \phi_{j+1,k}(x) = \sum_k c_k^j \phi_{j,k}(x) + \sum_k d_k^j \psi_{j,k}(x) = f^j + \delta^j, \quad (2.50)$$

where $c_k^j = \sum_s \langle \phi, \phi_{-1,s-2k} \rangle c_s^{j-1}$, $d_k^j = \sum_s \langle \psi, \phi_{-1,s-2k} \rangle c_s^{j-1}$, $c_k^0 = \langle f^0, \phi_{0,k} \rangle$. Here

$$f^j = \sum_k c_k^j \phi_{j,k}(x), \quad \delta^j = \sum_k d_k^{j-1} \psi_{j,k}(x)$$

are respectively called the approximate part and the detailed part of the signal. Following the above method, the original signal is decomposed to multi-scale signals, and the numbers of the data of all levels are equal.

Therefore, for the experimental data $\{x(t_i), t_i = t_0 + i\Delta t\}$, we measured in the field (the wind velocity and saltation activity), c_k^0 can be calculated using:

$$c_k^0 = \Delta t \sum_l x(t_l) \phi_{0,k}(t_l). \quad (2.51)$$

Here in, the approximate part and the detailed part of the original signal can be computed through Eq. 2.50.

It is found that the correlation dimension grows with the increasing of embedding dimension of phase space for different levels and different heights, so it can be concluded that the boundary turbulence beneath 2 m should be considered as a predominant random behavior rather than chaos.

In order to further analyze the fluctuating profile of the flow velocity and the saltation activity, some statistic of the experimental data $\{x(t_0 + i\Delta t) = \{x(i)\}$ are calculated.

average:
$$\bar{X} = \frac{1}{t_a} \sum_{i=1}^N x(t_i) = \frac{1}{N} \sum_{i=1}^N x(i), \quad (2.52)$$

standard deviation:
$$\sigma = \sqrt{\frac{1}{N-1} \sum_{i=1}^N [x(i) - \bar{X}]^2}, \quad (2.53)$$

skewness:
$$S_k = \frac{1}{\sigma^3 N} \sum_{i=1}^N [x(i) - \bar{X}]^3 \quad (2.54)$$

kurtosis:
$$K_x = \frac{1}{\sigma^4 N} \sum_{i=1}^N [x(i) - \bar{X}]^4, \quad (2.55)$$

and turbulence:
$$I = \sigma / \bar{X}. \quad (2.56)$$

Generally the total time length, $t_a = N\Delta t$, can be selected as 10 minutes to one hour and in our calculations $t_a = 30$ min. The statistics of the measured velocity data (including the data measured on the bare ground and on the dune crest) are listed in Table 2.1, and the same statistic for the wind velocity and the saltation activity are listed in Table 2.2, in which the measuring heights of the wind velocity and the saltation activity are 0.15 m and 0.04 m, respectively. The total data for two hours is divided into four groups according to the time period.

It can be shown from Table 2.1 that the mean wind gusts obey the logarithmic law, and they almost approach standard normal distribution at all heights ($S_k \approx 0$, $K_x \approx 3$). Also revealed by this table is that the Standard Deviation (STD) increases and the other parameters, such as the turbulence, the skewness and the kurtosis, all reduce as the height increases. Compared to the bare interdune results, the skewness and the kurtosis deviate more from normal distribution, which shows that the wind profile is more intermittent on the dune crest. From Table 2.2 we can see that the skewness and the kurtosis of the saltation activity get far away from a Gaussian distribution, indicating strong intermittent characteristics. The above analysis leads to the conclusion that although the wind in the period of the weather scale has important effects on the sediment transport (for example, it may be the dynamical cause of sand storms), the wind gusts in the turbulence scale directly affect the wind-blown sand transport process

Table 2.1. The statistics of the wind velocity

| | Height [m] | Average [m s ⁻¹] | STD | Turbulence | Skewness | Kurtosis |
|--------|---------------|---------------------------------|------|------------|----------|----------|
| Dune | 0.15 | 6.02 | 1.08 | 0.179 | 0.250 | 2.77 |
| | 0.55 | 7.81 | 1.34 | 0.172 | 0.262 | 2.60 |
| | 1.00 | 8.12 | 1.38 | 0.170 | 0.229 | 2.57 |
| | 2.00 | 8.52 | 1.42 | 0.167 | 0.212 | 2.34 |
| Ground | 0.12 | 5.38 | 1.10 | 0.204 | 0.129 | 2.76 |
| | 0.55 | 6.97 | 1.32 | 0.190 | 0.104 | 2.68 |
| | 1.00 | 7.53 | 1.42 | 0.188 | 0.079 | 2.70 |
| | 2.00 | 8.16 | 1.52 | 0.186 | 0.003 | 2.63 |

STD represents Standard deviation.

Table 2.2. The statistics of the wind velocity and the saltation activity

| N/Statistics | Average | STD | STD/average | Skewness | Kurtosis |
|--------------|---------|-------|-------------|----------|----------|
| I | 6.02 | 1.08 | 0.18 | 0.25 | 2.77 |
| | 10.51 | 14.94 | 1.42 | 2.84 | 14.71 |
| II | 6.02 | 1.08 | 0.18 | 0.30 | 2.96 |
| | 9.57 | 13.77 | 1.44 | 2.91 | 16.18 |
| III | 6.30 | 1.05 | 0.17 | 0.46 | 3.52 |
| | 15.73 | 22.01 | 1.40 | 3.25 | 17.34 |
| IV | 6.20 | 0.91 | 0.15 | 0.14 | 2.95 |
| | 16.82 | 19.86 | 1.18 | 2.79 | 16.60 |

I-IV is the group number. In each group, the first line represents wind velocity, and the second line is saltation activity.

near the Earth's surface through momentum exchange with erodible surfaces (see Fig. 2.15).

In order to define the time scale related to the sand transport process, the Mid-Smoothing Method is used. The value at time $k\Delta t$ is

$$X_s(k) = \frac{1}{2m_s + 1} \sum_{i=k-m_s}^{k+m_s} x(i), \quad k = m_s + 1, m_s + 2, \dots, N - m_s.$$

Here $\{x(t_0 + i\Delta t) = \{x(i)\}$ is experimental data series, $T_s = (2m_s + 1)\Delta t$ is the smooth period. Then the variance of the smoothed wind velocity (measured at 0.15 m) and the saltation activity (measured at 4 cm) are calculated for different time periods. The results show that the cross-correlation coefficient of the two variance series gets the largest value for 3minute periods, which implies that the wind gusts in this time scale contribute the most to the sand erosion process. Similarly, Butterfield (1991) found that the responding time of the flow to the sand flux is 6–20 s, while Neumann et al. (2000) got a period of about 5–20 min through a power spectrum analysis method. The wind gusts found in our work or Neumann et al. (2000) are actually wind gusts. Zeng et al. (2007) revealed that the wind gusts of 3–5 min have some kind of coherent structure and our work shows that the wind gusts with coherent structure not only are related directly to the dust entrainment process in the region of 47–280 m, but they may also affect the movement of the Earth's surface sands.

2.6.2 Prediction Model I: Wind Gusts Vary with Time

We define T_g as the wind gusts period which represents the duration between two successive time points on which the wind velocity passes its mean value \bar{u} . Assume that the frequency approximates to its probability, i.e.,

$$f(T_g) = \frac{1}{N_g} \Delta N_g(T_g \leq T_e < T_g + \Delta T_g). \quad (2.57)$$

N_g is the total number of the periods, T_e is the wind gusts period calculated from the experimental data. Fig. 2.16 shows the variations of T_e in 30 min and they are computed from the wind velocity data at 2.0 m height, n_e is the series number of T_e . It is found that T_g follows an exponential distribution, expressed as

$$f(T_g) = \frac{1}{a} \exp\left(-\frac{T_g}{a}\right), \quad (2.58)$$

where the parameter a is about 5.0.

From Fig. 2.17 we can see that the wind variations show abrupt characteristics, making it seem to be the discontinuous square-wave function rather than a sine or cosine function. In shorter periods (5 min) the experimental data still shows small oscillations, which is called noise and can be represented by a Gaussian distribution with a standard deviation pre-specified.

Then suppose the wind velocity at the reference height has the following form:

$$u = \bar{u} + \langle u \rangle + u', \quad (2.59)$$

where \bar{u} is the mean velocity, $\langle u \rangle$, u' represent the turbulence fluctuations and the Gaussian noise respectively, where the turbulence fluctuations is simply expressed by a square wave function. The amplitude of the square wave is defined as Gm . We assume $Gm = \text{sign}(T_g)MT_g$, where $\text{sign}(T_g)$ is selected to make two successive period have an opposite sign, M is a parameter, which is calculated through introducing the ratio γ of the turbulence energy and the total energy and can be represented by the variance of the square wave function and the variance of the wind flow, T_g is denoted by a random number which obey the exponential distribution

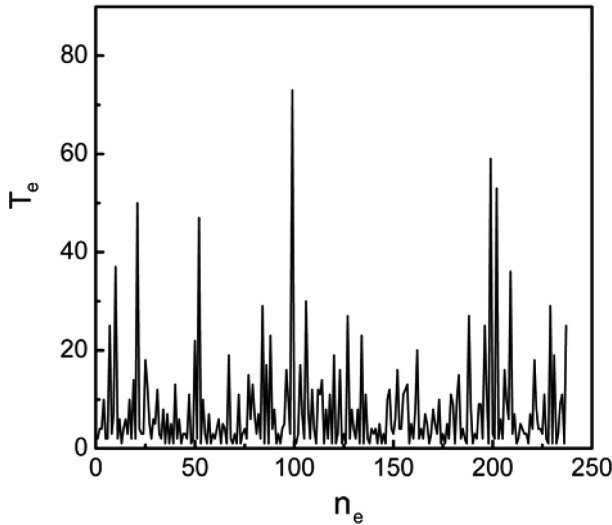


Fig. 2.16. Wind gusts period occurs in 30 minutes. T_e is the wind gusts period calculated from the experimental data, n_e is the series number of T_e . (the experimental data was measured by the author et al. on flat ground in Minqin, China, on November 2, 2007)

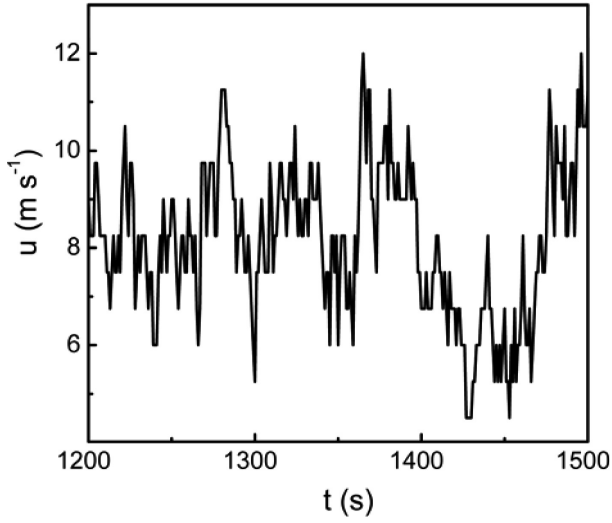


Fig. 2.17. Variations of wind velocity in 5 minutes (measured by the author et al. on flat ground in Minqin, China, on November 2, 2007)

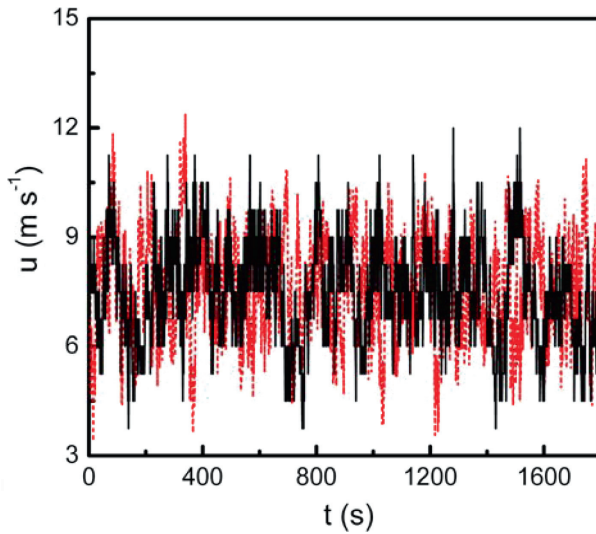


Fig. 2.18. Wind velocity predicted by Eq. 2.59 with $a=5.0$ and $\gamma \approx 0.8$ (red dot line) compared with the experimental data at 2.0 m (black solid line) measured by the author et al. on flat ground in Minqin, China on November 2, 2007

with a parameter of 5.0. The noise is represented by random numbers to follow a Gaussian distribution, the standard deviation is specified as $\sigma_r = \sqrt{\sigma_u^2(1-\gamma)}$. In the modeling, we first choose a γ and the initial value of M , then change M continuously until the sum of the variance of the square wave function and the variance of the Gaussian noise equals the total variance σ_u^2 , which is given as a model parameter.

Based on the average value and variance of experimental data measured at 2 m, the temporal variation of the wind velocity is simulated, in which $\gamma \approx 0.8$. It is found that the predicted velocity has a satisfactory agreement with experimental results (see Fig. 2.18).

2.6.3 Prediction Model II: Wind Gusts Vary with Height

We choose the wind velocity at 2.0 m as the reference wind velocity to generate the wind velocity beneath it. The difference between the velocity $u_h(h, t_i)$ at a height of h below 2 m and the reference wind velocity at time t_i is defined as u'' , then $u'' = u_r(h_r, t_i) - u_h(h, t_i)$, where h_r is the reference height while $u_r(h_r, t_i)$ is the corresponding wind velocity, then the mean of u'' is:

$$\bar{u}'' = \overline{u_r(h_r, t_i) - u_h(h, t_i)} = \overline{u_r(h_r, t_i)} - \overline{u_h(h, t_i)}. \quad (2.60)$$

Suppose the mean velocity obeys the logarithmic law, then through rewriting Eq. 2.60 we get:

$$\bar{u}'' = \frac{u^*}{k} \ln \frac{h_r}{z_0} - \frac{u^*}{k} \ln \frac{h}{z_0} = \frac{u^*}{k} \ln \frac{h_r}{h} = \frac{u^*}{k} \ln \frac{2.0}{h}. \quad (2.61)$$

So it is assumed that $\bar{u}'' = k_1 \ln(2.0/h) + k_2$, k_1, k_2 is to be determined based on experimental data, and the variance of u' is:

$$\sigma_{\Delta h}^2 = \overline{\left[(u_r - u_h) - (\bar{u}_r - \bar{u}_h) \right]^2} = \overline{(u'_r - u'_h)^2} = \overline{u'^2_r} + \overline{u'^2_h} - 2\overline{u'_r u'_h}.$$

Since $\overline{u'^2_r} = \sigma_r^2$, $\overline{u'^2_h} = \sigma_h^2$, if $\overline{u'_r u'_h} \approx \sigma_r \sigma_h$ is assumed, we get $\sigma_{\Delta h} = \sigma_r - \sigma_h$. According to Table 2.1, the turbulence does not change much with height, and we can suppose it keeps a constant near the surface, so:

$$I_h = I_r \quad \text{or} \quad \frac{\sigma_h}{\bar{u}_h} = \frac{\sigma_r}{\bar{u}_r}, \quad (2.62)$$

then $\sigma_{\Delta h} = \sigma_r - \sigma_h \propto \bar{u}_r - \bar{u}_h$, and we have $\sigma_{\Delta h} = k_3 \ln(2.0/h) + k_4$. k_3 and k_4 are also determined by the experimental data. On the basis of the wind ve-

locity measured on the bare ground, we get: $k_1 = 2.37u_* + 0.07$, $k_2 = -0.3$, $k_3 = 0.06$, $k_4 = 0.56$.

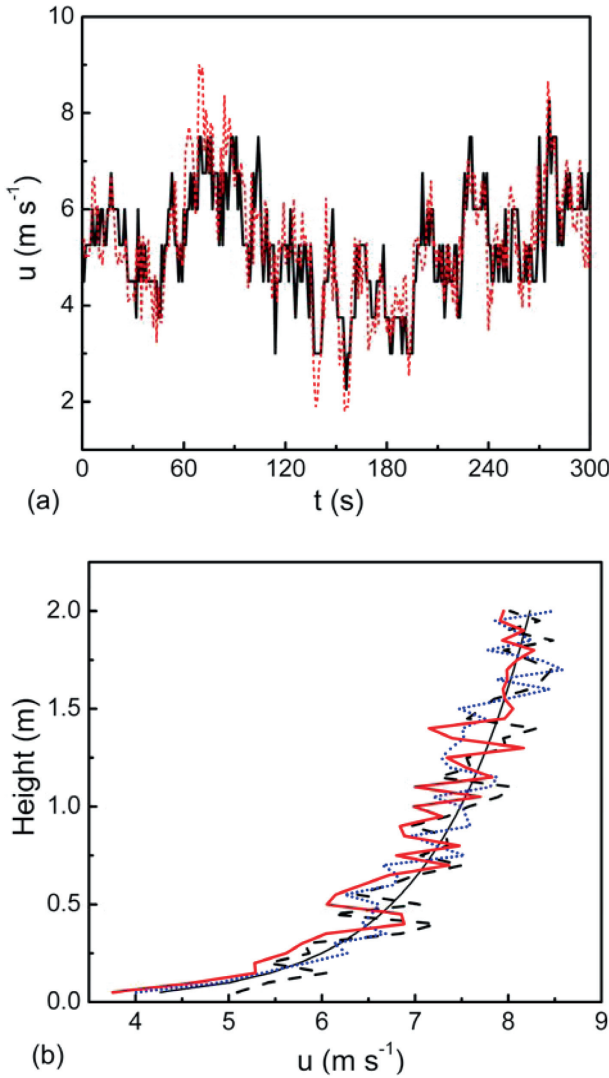


Fig. 2.19. (a) Comparison between results (---) predicted by the prediction model II (i.e., Eqs. 2.60 and 2.63) and experimental data (—) at 0.12 m which is the same as in Fig. 2.16, (b) Comparison between predicted wind profile (using model II, i.e., Eqs. 2.60 and 2.63, but change the height h continuously) and log-linear profile, in which the dash line (---), dot line (.....) and solid line represent the wind gusts at t_0 , $t_0 + \Delta t$, $t_0 + 2\Delta t$

In this context, we assume u'' obeys a Gaussian distribution

$$f(u'') = \frac{1}{\sqrt{2\pi}\sigma_{\Delta h}} \exp\left[-\frac{(u'' - \bar{u}'')^2}{\sigma_{\Delta h}^2}\right], \quad (2.63)$$

then we can calculate the wind gusts varying with height. Fig. 2.19a displays the comparison between the predicted and experimental wind velocity at 0.12 m. It can be seen that these two velocities agree very well. Then we give a prediction on the wind velocity varying with height in three successive seconds (Fig. 2.19b). From Fig. 2.19b it can be seen that the velocity distribution with height does not follow the logarithmic law and this deviation can attain $2\text{--}3 \text{ m}\cdot\text{s}^{-1}$. This proves that the consideration of wind gusts is essential.

Mechanics of Wind-blown Sand Movements

Zheng, X.

2009, XX, 309 p. 163 illus., 58 illus. in color., Hardcover

ISBN: 978-3-540-88253-4